Title: Structural basis of epitope selectivity and potent protection from malaria by PfCSP antibody L9

One sentence summary: The L9 light chain is crucial for potency by conferring multivalent, high affinity binding to the NPNV minor repeats of PfCSP.

Authors: Gregory M. Martin[1], Monica L. Fernández Quintero[2], Wen-Hsin Lee[1], Tossapol Pholcharee[1]†, Lisa Eshun-Wilson[1], Klaus R. Liedl[2], Marie Pancera[3], Robert A. Seder[4], Ian A. Wilson[1,5], Andrew B. Ward[1]

Affiliations:

[1]Department of Integrative Structural and Computational Biology, The Scripps Research Institute; La Jolla, CA 92037; USA.

[2]Department of General, Inorganic, and Theoretical Chemistry, Center for Chemistry and Biomedicine, The University of Innsbruck; Innrain 80-82/III, 6020 Innsbruck, Austria.

[3]Vaccine and Infectious Disease Division, Fred Hutchinson Cancer Research Center; Seattle, WA 98109; USA.

[4]Vaccine Research Center, National Institute of Allergy and Infectious Diseases, National Institutes of Health; Bethesda, MD 20892; USA.

[5]The Skaggs Institute for Chemical Biology, The Scripps Research Institute; La Jolla, CA 92037; USA.

†Present address: Department of Biochemistry; University of Oxford; Oxford OX1 3DR; UK.

Abstract:

A primary objective in malaria vaccine design is the generation of high-quality antibody responses against the circumsporozoite protein of the malaria parasite, *Plasmodium falciparum* (PfCSP). To enable rational antigen design, we solved a cryo-EM structure of the highly potent anti-PfCSP antibody L9 in complex with recombinant PfCSP. We found that L9 Fab binds multivalently to the CSP minor (NPNV) repeats, which is stabilized by a novel set of affinity-matured homotypic, antibody-antibody contacts. Molecular dynamics simulations revealed a critical role of the L9 light chain in integrity of the homotypic interface, which likely impacts CSP affinity and protective efficacy. These findings reveal the molecular mechanism of the unique NPNV selectivity of L9 and emphasize the importance of anti-homotypic affinity maturation in protective immunity against *P. falciparum*.

47 **Main Text:**

48 Malaria remains one of the world's deadliest infectious diseases, and in 2021 was responsible for
49 241 million clinical infections and 627,000 deaths worldwide (*1*), primarily among young
50 children in sub-Saharan Africa. RTS,S/AS01B (RTS,S), the only approved malaria vaccine, is
51 only partially effective, providing ~30% protection from clinical infection after four years in
52 children aged 5-17 months (*2, 3*). Thus new tools, like next-generation vaccines and highly
53 potent monoclonal antibodies (mAbs), the latter of which can provide prolonged, sterilizing
54 immunity, are needed for prevention and elimination of malaria.
55
56 PfCSP, the primary surface antigen of *P. falciparum* sporozoites, is a major target for vaccines and
57 mAbs as it is both highly conserved and critical for the initiation of malaria infection. PfCSP
58 contains an immunodominant central repeat region composed of repeating four-amino-acid units,
59 structurally defined as DPNA, NPNV, and NPNA (*4-11*). These roughly define the junctional,
60 minor repeat, and major repeat epitopes, respectively. Each epitope can generate potent antibodies
61 that prevent malaria infection in animal models (*12-14*), with the junctional mAb cis43LS
62 demonstrating high-level protection against controlled human malaria infection (CHMI) in
63 humans (*15*). Recently, we identified the minor-repeat-specific mAb L9 as one of the most potent
64 anti-PfCSP mAbs isolated to date (*16*), which can also confer high-level sterilizing immunity
65 against CHMI in humans (*17*). Like many of the most potent NPNA-specific mAbs, L9 is also
66 encoded by the *IGHV3-33*/*IGKV1-5* heavy/light chain gene combination. However, L9 is highly
67 specific for the NPNV (minor) repeats and relies on critical contributions from the light chain for
68 both NPNV selectivity and high potency (*6*).
69

To understand the molecular basis of these unique functional properties, we solved a 3.36 Å cryo-EM structure of L9 Fab in complex with a recombinant PfCSP construct, rsCSP, which contains the full N-terminal, junctional, and C-terminal regions, and about half the number of NPNA repeats as the 3D7 reference strain (Fig. 1, fig. S1, table S1). In the cryo-EM map, we observe three tightly packed Fabs bound to a central rsCSP, with each Fab simultaneously interacting with the peptide and the adjacent Fab via homotypic interactions (*8, 11, 18, 19*). In general, the complex is homogeneous and the density is well-resolved for each L9 variable region (Fv) as well as the rsCSP peptide (Fig. 1B). The structure of rsCSP, built *de novo* based on the EM density, consists solely of the minor repeat region (Fig. 1F). The modeled antigen sequence comprises 26 residues encompassing three complete NPNV and DPNA repeats, i.e. NA$(NPNVDPNA)_3$; there is no additional density observed that would correspond to N-terminal, C-terminal, or major repeat regions. The L9 Fab and peptide cryo-EM structures correspond well with our recent X-ray structures of two chimeric precursors of L9 ($L9_K/F10_H$ and $F10_K/L9_H$) in complex with a short minor repeat peptide (NANPNVDP) (*6*) (fig. S2). Relative to the L9 cryo-EM structure, RMSD values for both chimeric Fvs are ~0.5Å, and ~0.1Å over the NPNV peptide.

In the cryo-EM structure, each L9 Fab primarily engages a single NPNV repeat, while the DPNA repeats are largely unbound and serve as a linker between each NPNV (Fig. 1C and E). Thus, the full epitope bound by a single L9 Fab is NPNVD (Fig. 1G). Each NPNV motif adopts a type 1 β-turn, which is frequently observed for DPNA and NPNA motifs bound to anti-PfCSP antibodies from a variety of heavy chain lineages (*4, 8, 20*). The DPNA repeats in the L9 structure, however, are more extended and lack clear secondary structure elements (Fig. 1,F and H). The L9 epitope is centered on the NPNV type 1 β-turn, which resides in a deep, central pocket on the Fab formed

primarily from CDRL1, CDRL3, and CDRH3, with smaller contributions from CDRH1 and H2 (Fig. 2A). Interestingly, overall buried surface area (BSA) on L9 is slightly biased toward the light chain (LC; $L9_K$) (fig. S3, A and B). Of the 550Å^2 total BSA on a single L9 Fab, $L9_K$ contributes 294 Å^2 (53.5%), while the heavy chain (HC; $L9_H$) contributes 256Å^2 (46.5%), indicating a critical role of $L9_K$ in PfCSP binding.

As frequently observed in anti-NPNA major repeat mAbs, many direct antigen contacts are with germline-encoded aromatic residues, which in L9 create a hydrophobic cage surrounding the NPNV motif (Fig. 2B, table S2). In particular, $W32^L$ in CDRL1 stacks closely against the N-terminal Asn of the NPNV motif (N1) forming a CH-π bond, while $Y94^L$ in CDRL3 engages the repeat Pro (P2) (Fig. 2C, fig. S3, C and D). L9 also utilizes the strictly conserved *IGHV3-33* germline residue $W52^H$ in CDRH2, which in all structures of *IGHV3-33* mAbs solved to date forms a critical CH-π interaction with P6 of the second NPNA repeat in the $NPNA_2$ epitope (*7, 8, 11, 20*). However, in L9, this role is assumed by $Y94^L$, and $W52^H$ principally acts to stabilize the $Y94^L$:P2 interaction through a π-π stacking interaction with the $Y94^L$ side chain (Fig. S3D-F).

This paratope structure is distinct from most other *IGHV3-33* mAbs targeting both major and minor repeats. In L9, a repositioning of the HC and LC CDR3 loops, along with a rearrangement of $W52^H$ and CDRH2, creates a compact, central CSP binding pocket bounded by each of the HC and LC CDRs (Fig. 2B). A somatically mutated residue, $R96^L$ in CDRL3, is found at the base of the pocket and creates a highly basic cavity (Fig. S3G). This basic binding pocket is nearly fully occupied by the N3 side chain, which forms key H-bonds with $R96^L$ (Fig. 2C), while V4 occupies a hydrophobic cavity at the interface of CDRL1, L3, and CDRH3 (fig. S3C). With this unique

CDR conformation, L9 appears optimally disposed to bind the bulkier minor repeat residue V4, which is the only difference between the NPNA and NPNV epitopes.

Another unique property of L9 is the ability to "crosslink" two NPNV motifs within the minor repeat region of PfCSP, which improves binding affinity (*6*). Our cryo-EM structure reveals that L9 achieves this through multivalent Fab binding to sequential NPNV repeats stabilized by an extensive antibody-antibody, or homotypic, interface between adjacent Fabs (Fig. 3A). Homotypic interactions have now been identified in several anti-NPNA mAbs and appear to be a characteristic feature of the *IGHV3-33* antibody family (*8, 11, 18-20*). Importantly, we demonstrate L9 as the first non-NPNA targeting anti-PfCSP mAb to also utilize homotypic interactions, suggesting that both the major and minor PfCSP repeats can facilitate their development.

The L9 homotypic interface is distinct from that observed in NPNA-specific *IGHV3-33* mAbs, which is generally conserved and derives primarily from the heavy chain (*11, 19*) (fig. S5). In contrast, $L9_K$ contributes numerous critical homotypic contacts, and total BSA in the interface is evenly distributed between heavy and light chains (905Å^2 and 839Å^2, respectively) (Fig. 3, E and F). In the cryo-EM structure, $L9_K$ of FabC packs tightly against $L9_H$ of FabB, and extensive polar and hydrophobic contacts are made between CDRL1 and the LC framework region 3 of FabC (LFR3) with HFR1, CDRH1, and CDRH3 of FabB (Fig. 3A; fig. S4; table S3). The interface between FabB and FabA is nearly identical. Importantly, several residues mediating critical homotypic interactions (Fig. 3, B to D) correlate with somatic hypermutation of the germline *IGHV3-33* and *IGKV1-5* genes (Fig. 3E and F; fig. S5). Four somatically mutated residues in $L9_K$,

138 $F28^{L}$ and $R31^{L}$ in CDRL1, and $E68^{L}$ and $H70^{L}$ in LFR3, account for the majority of BSA
139 contributed by the LC to the homotypic interface (Fig. 3E).
140
141 $E68^{L}$ lies at the core of the homotypic interface in L9, where it forms a key salt bridge with the
142 germline-encoded $R94^{H}$ of $CDRH3_{B}$ (Fig. 3B; fig. S4). In $L9_{H}$, $R94^{H}$ forms a conserved interaction
143 with $Y102^{H}$ to stabilize the base of CDRH3; thus $E68^{L}$ may also indirectly impact antigen binding
144 through stabilization of the CDRH3 loop in the adjacent Fab. $F28^{L}$ coordinates a series of π-π
145 stacking interactions in the opposing $CDRH1_{B}$ ($Y32^{H}$) and $CDRH3_{B}$ ($F96^{H}$ and $F100c^{H}$) while also
146 packing against the $E68^{L}$ side chain. This pi network culminates in a cation-π bond between $R31^{L}$
147 from $CDRL1_{C}$ and $F100c^{H}$ from the opposing $CDRH3_{B}$ (Fig. 3C). On the other side of the
148 homotypic interface from $E68^{L}$, a mutated framework residue $H70^{L}$ forms a hydrogen bond with
149 the side chain of $Q1^{H}$ in FabA in addition to multiple van der Waals contacts with $CDRH1_{B}$ (Fig.
150 3D). Each of these homotypic contacts are not encoded in the germline sequence, and none directly
151 contact rsCSP (fig. S3, A and B). These findings provide strong evidence for affinity maturation
152 to optimize antibody-antibody binding, which may in turn enhance CSP avidity and protective
153 efficacy, as we have shown recently for multiple NPNA-specific *IGHV3-33* mAbs (*11*).
154
155 The four somatic mutations in $L9_{K}$ are atypical: $F28^{L}$, $E68^{L}$, and $H70^{L}$ are observed in less than
156 1% percent of all human *IGKV1* light chain sequences, while $R31^{L}$ is observed in only 2% (Fig.
157 S5A) (*21*). Strikingly, F28 and H70 also correspond to two of the five amino-acid differences
158 between mature L9 and the chimeric L9 mAb $F10_{K}/L9_{H}$ (S28 and D70 in $F10_{K}$). As F28 and H70
159 both mediate key homotypic interactions in L9, which would likely be lost in $F10_{K}$, these residues
160 may explain the functional differences of $F10_{K}/L9_{H}$ from L9, namely (1) reduced avidity to CSP

minor repeats, (2) loss of the ability to bind two adjacent NPNV repeats, and (3) significantly reduced protection *in vivo* (p<0.001) (*6*).

To test this hypothesis, and to understand the role of homotypic contacts in $L9_K$ in general, we used molecular dynamics simulations to characterize WT L9 and a series of $L9_K$ variants. $L9_K$ residues were reverted to either the germline *IGKV1-5* gene (R31S, E68G) or to the $L9_K$ precursor $F10_K$ (F28S, H70D). We first compared the free energy landscapes of the CDR loops of individual Fv domains unbound to rsCSP (Fig. 4; fig. S6). We find that the R31S, E68G and H70D mutations in $L9_K$ result in a broader conformational space and additional highly probable minima compared to the WT L9 Fv, indicating that these residues are critical for determining the shape and the conformational flexibility of the paratope (Fig. 4, B and C; fig. S6). These minima correspond to a substantial shift away from the binding competent conformation in combination with a higher conformational entropy, suggesting a decrease in stability and/or binding affinity (Fig. 4D). Importantly, when combined (R31S-E68G-H70D), these mutations significantly destabilize the homotypic interface (table S4; p<0.001), substantiating their key role in mediating homotypic interactions. Interestingly, the H70D single mutant *stabilizes* the homotypic interface (table S4), suggesting the germline E70 or $F10_K$ D70 may have initialized the evolution of homotypic interactions during L9 maturation. Unlike other LC mutants, the F28S Fv reveals a similar conformational space and diversity in the CDR loops compared to the WT L9 Fv. However, F28S leads to formation of a new *intra*molecular salt bridge between residues $R31^L$ and $E68^L$, with simultaneous loss of the *inter*molecular salt bridge between $E68^L$ and $R94^H$ and the cation-π bond between $R31^L$ and $F100c^H$ (Fig. 4A). Thus, in addition to direct homotypic interactions, F28 acts indirectly through $E68^L$ and $R31^L$ to further stabilize antibody-antibody binding. This is reflected

in the significantly decreased interaction energies of the homotypic interface in the F28S mutant relative to WT L9 (table S4) and is visualized in Movie S1. To understand the molecular basis of key functional differences between L9 and F10, we next modelled the F10 chimeras in the context of the trimeric Fab-rsCSP complex. Compared to WT L9 and $L9_K/F10_H$, the homotypic interface is strongly destabilized in $F10_K/L9_H$ (table S4). This suggests that $F10_K/L9_H$ would not bind multivalently to the minor repeats and would have overall reduced binding affinity, which is consistent with our previous functional data on this chimera (*6*). Five residues differ between $L9_K$ and $F10_K$: F28S, L33V, P40A, H70D, and E90Q (Fig. 3E). We find that the F28S mutation alone accounts for ~80% of the destabilization of the homotypic interface observed with $F10_K/L9_H$ compared to WT L9, while the H70D single mutant and the L33V-P40A-E90Q triple mutant Fvs both slightly *increase* stability of the complex (table S4). Taken together, these data suggest that the dramatic destabilization seen in MD simulations of the $F10_K/L9_H$ chimera is primarily the result of the F28S mutation. Therefore, this rare mutation in $L9_K$ (S28F), and the network of homotypic contacts it mediates, may underlie the key functional differences between L9 and $F10_K/L9_H$.

Overall, this study reveals the structural basis for the extraordinary selectivity and binding affinity of L9 for the NPNV minor repeats and highlights the critical role of $L9_K$ for both functions. We find that rare, somatically mutated residues in $L9_K$ mediate extensive homotypic contacts between adjacent L9 Fabs and thus multivalent binding to adjacent NPNV motifs. These contacts underscore the requirement of at least two NPNV motifs for high affinity CSP binding by L9 (1000 nM vs 13 nM for CSP peptides with one and two NPNV, respectively) (*6*); Based on our recent finding that affinity-matured homotypic interactions in three potent NPNA-specific *IGHV3-33* mAbs are critical for both high NPNA avidity and protective efficacy (*11*), it is likely that $L9_K$-

mediated homotypic interactions are also critical for the potency of L9. Notably, these $L9_K$ residues (F28, R31, E68, H70) make no direct contacts with rsCSP (fig. S3; table S2), indicating that the minor repeat region facilitates antibody-antibody affinity maturation in the context of multiple adjacent NPNV motifs, as has been observed for extended NPNA repeats (*11, 18, 19*). L9 is one of the most potent anti-PfCSP mAbs and is currently undergoing clinical development as a monoclonal therapy for malaria prevention (*17*). Thus, these structural data will be useful for rational antibody engineering to improve both the protective efficacy and pharmacokinetic properties of this mAb. The discovery of L9 and the NPNV minor repeat region as a highly protective epitope on PfCSP has led to new efforts to re-design PfCSP-based vaccines to elicit L9-like antibodies (*22, 23*). The cryo-EM structure presented here now enables a structure-based approach, which may be instrumental in developing the next-generation malaria vaccine. Future studies to identify related, NPNV-specific mAbs should enhance our understanding of this class of antibodies and their important contribution to protective immunity against malaria.

REFERENCES AND NOTES:

1. Geneva: World Health Organization (2021). World malaria report 2021. License: CC BY-NC-SA 3.0 IGO. pp. xv-xvi.
2. RTS,S Clinical Trials Partnership *et al.*, First results of phase 3 trial of RTS,S/AS01 malaria vaccine in African children. *N Engl J Med* **365**, 1863-1875 (2011).
3. RTS,S Clinical Trials Partnership, Efficacy and safety of RTS,S/AS01 malaria vaccine with or without a booster dose in infants and children in Africa: final results of a phase 3, individually randomised, controlled trial. *Lancet* **386**, 31-45 (2015).

4. N. K. Kisalu *et al.*, A human monoclonal antibody prevents malaria infection by targeting a new site of vulnerability on the parasite. *Nat Med* **24**, 408-416 (2018).

5. J. Tan *et al.*, A public antibody lineage that potently inhibits malaria infection through dual binding to the circumsporozoite protein. *Nat Med* **24**, 401-407 (2018).

6. L. T. Wang *et al.*, The light chain of the L9 antibody is critical for binding circumsporozoite protein minor repeats and preventing malaria. *Cell Rep* **38**, 110367 (2022).

7. D. Oyen *et al.*, Structural basis for antibody recognition of the NANP repeats in Plasmodium falciparum circumsporozoite protein. *Proc Natl Acad Sci U S A* **114**, E10438-E10445 (2017).

8. T. Pholcharee *et al.*, Structural and biophysical correlation of anti-NANP antibodies with in vivo protection against P. falciparum. *Nat Commun* **12**, 1063 (2021).

9. T. Pholcharee *et al.*, Diverse Antibody Responses to Conserved Structural Motifs in Plasmodium falciparum Circumsporozoite Protein. *J Mol Biol* **432**, 1048-1063 (2020).

10. D. Oyen *et al.*, Structure and mechanism of monoclonal antibody binding to the junctional epitope of Plasmodium falciparum circumsporozoite protein. *PLoS Pathog* **16**, e1008373 (2020).

11. G. M. Martin *et al.*, Affinity-matured homotypic interactions induce spectrum of PfCSP-antibody structures that influence protection from malaria infection. *bioRxiv* **doi: https://doi.org/10.1101/2022.09.20.508747** (2022).

12. Y. Flores-Garcia *et al.*, Optimization of an in vivo model to study immunity to Plasmodium falciparum pre-erythrocytic stages. *Malar J* **18**, 426 (2019).

13. R. Raghunandan *et al.*, Characterization of two in vivo challenge models to measure functional activity of monoclonal antibodies to Plasmodium falciparum circumsporozoite protein. *Malar J* **19**, 113 (2020).

14. Y. Flores-Garcia *et al.*, The P. falciparum CSP repeat region contains three distinct epitopes required for protection by antibodies in vivo. *PLoS Pathog* **17**, e1010042 (2021).

15. M. R. Gaudinski *et al.*, A Monoclonal Antibody for Malaria Prevention. *N Engl J Med* **385**, 803-814 (2021).

16. L. T. Wang *et al.*, A Potent Anti-Malarial Human Monoclonal Antibody Targets Circumsporozoite Protein Minor Repeats and Neutralizes Sporozoites in the Liver. *Immunity* **53**, 733-744 e738 (2020).

17. R. L. Wu *et al.*, Low-Dose Subcutaneous or Intravenous Monoclonal Antibody to Prevent Malaria. *N Engl J Med* **387**, 397-407 (2022).

18. K. Imkeller *et al.*, Antihomotypic affinity maturation improves human B cell responses against a repetitive epitope. *Science* **360**, 1358-1362 (2018).

19. D. Oyen *et al.*, Cryo-EM structure of P. falciparum circumsporozoite protein with a vaccine-elicited antibody is stabilized by somatically mutated inter-Fab contacts. *Sci Adv* **4**, eaau8529 (2018).

20. R. Murugan *et al.*, Evolution of protective human antibodies against Plasmodium falciparum circumsporozoite protein repeat motifs. *Nat Med* **26**, 1135-1145 (2020).

21. M. B. Swindells *et al.*, abYsis: Integrated Antibody Sequence and Structure-Management, Analysis, and Prediction. *J Mol Biol* **429**, 356-364 (2017).

22. L. Jelinkova *et al.*, A vaccine targeting the L9 epitope of the malaria circumsporozoite protein confers protection from blood-stage infection in a mouse challenge model. *NPJ Vaccines* **7**, 34 (2022).

23. M. D. Langowski *et al.*, Restricted valency (NPNA)n repeats and junctional epitope-based circumsporozoite protein vaccines against Plasmodium falciparum. *NPJ Vaccines* **7**, 13 (2022).

Acknowledgments:

The authors thank B. Anderson for maintenance and administration of the cryo-EM facility at The Scripps Research Institute, and H.L. Turner and C.A. Bowman for technical support. We also thank L.T. Wang and N.K. Hurlburt for sharing of reagents and insightful discussions, and J.R. Riccabona and Y. Wang for fruitful discussions and technical support. The computational results presented here have been achieved (in part) using the Vienna Scientific Cluster (VSC). We acknowledge PRACE for awarding us access to Piz Daint at CSCS, Switzerland.

Funding: National Institutes of Health grant 1F32AI150216-01A1 (GMM); The Bill and Melinda Gates Foundation grant INV-004923 (IAW, ABW); Austrian Academy of sciences APART-MINT postdoctoral fellowship, Austrian Science Fund grant: P34518 (MFQ).

Author contributions: GMM, MP, RAS, IAW, and ABW conceived the project. GMM, MFQ, WHL, and TP designed and performed experiments, and analyzed the data. LEW analyzed data. KRL, MP, RAS, IAW, and ABW acquired funding and supervised the project. GMM and MFQ wrote the original manuscript draft. All authors contributed to manuscript review and editing.

Competing interests: The authors declare they have no competing interests.

Data and materials availability: The coordinates for the L9-rsCSP structure and the corresponding cryo-EM map have been deposited to the Protein Data Bank (PDB) and Electron Microscopy Data Bank (EMDB), respectively, with the accession codes 8EH5 and EMD-28135.

Supplementary Materials

Materials and Methods

Figures S1-S4

Tables S1-S4

References 23-58

Movie S1

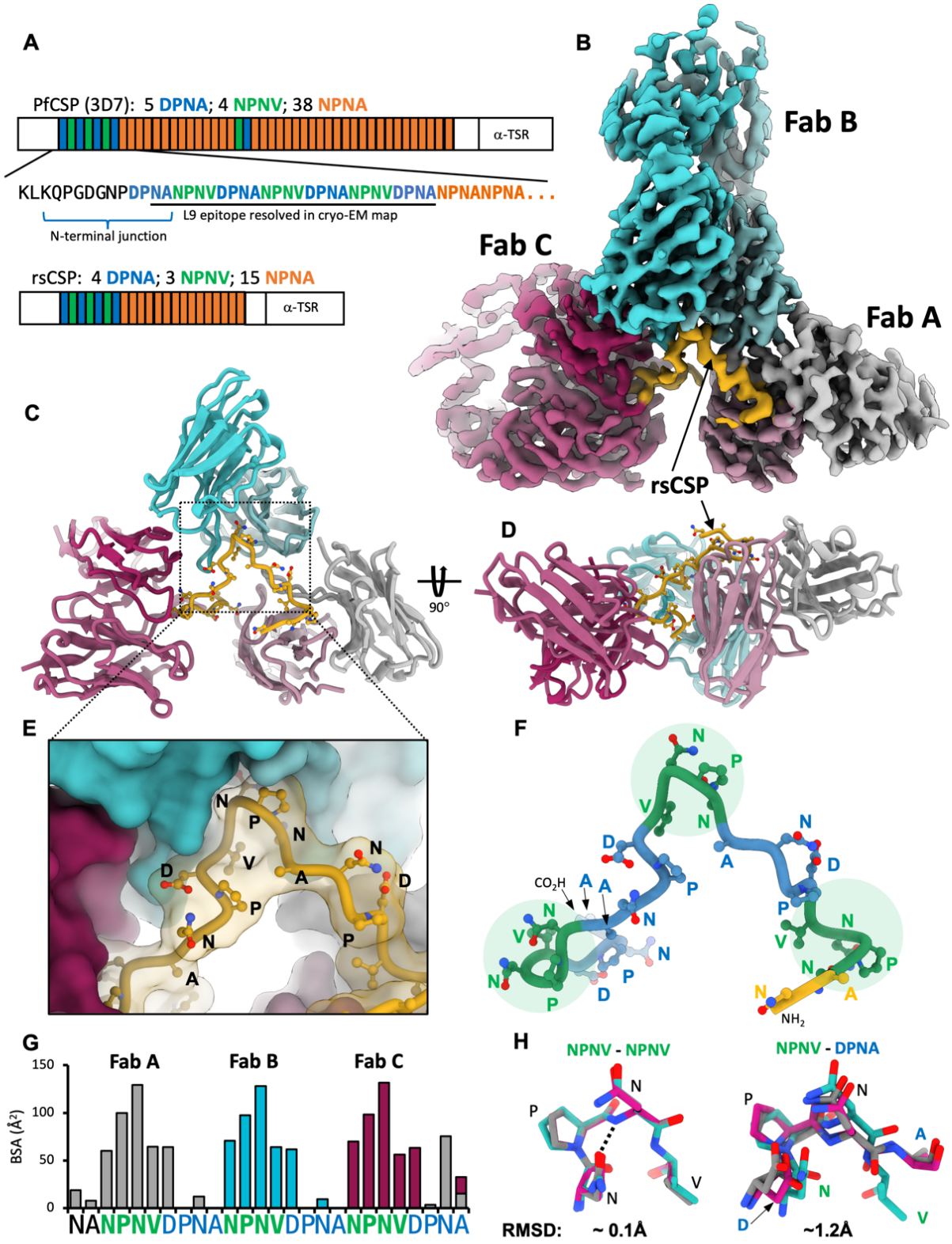

311

Figure 1. Cryo-EM structure of the L9 Fab-rsCSP complex. (A) Schematic of protein sequence of full-length PfCSP and rsCSP (recombinant). Each box corresponds to a single repeat. The minor repeat region is in blue and green. **(B)** Cryo-EM map of L9-rsCSP at 3.36Å. **(C)** Ribbon diagram of the atomic model; only the Fab variable region (Fv) was built into the density. **(D)** Rotated view of (C). **(E)** Zoomed-in view of (C), shown in a surface representation. **(F)** Model of the minor repeat peptide, colored as in (A). NPNV type-1 β-turns are highlighted with a green circle. **(G)** Buried surface area on rsCSP, color-coded to the Fab with which each rsCSP residue interacts. **(H)** Alignment of the three NPNV motifs (left), or the three DPNA motifs aligned to the central NPNV motif (right).

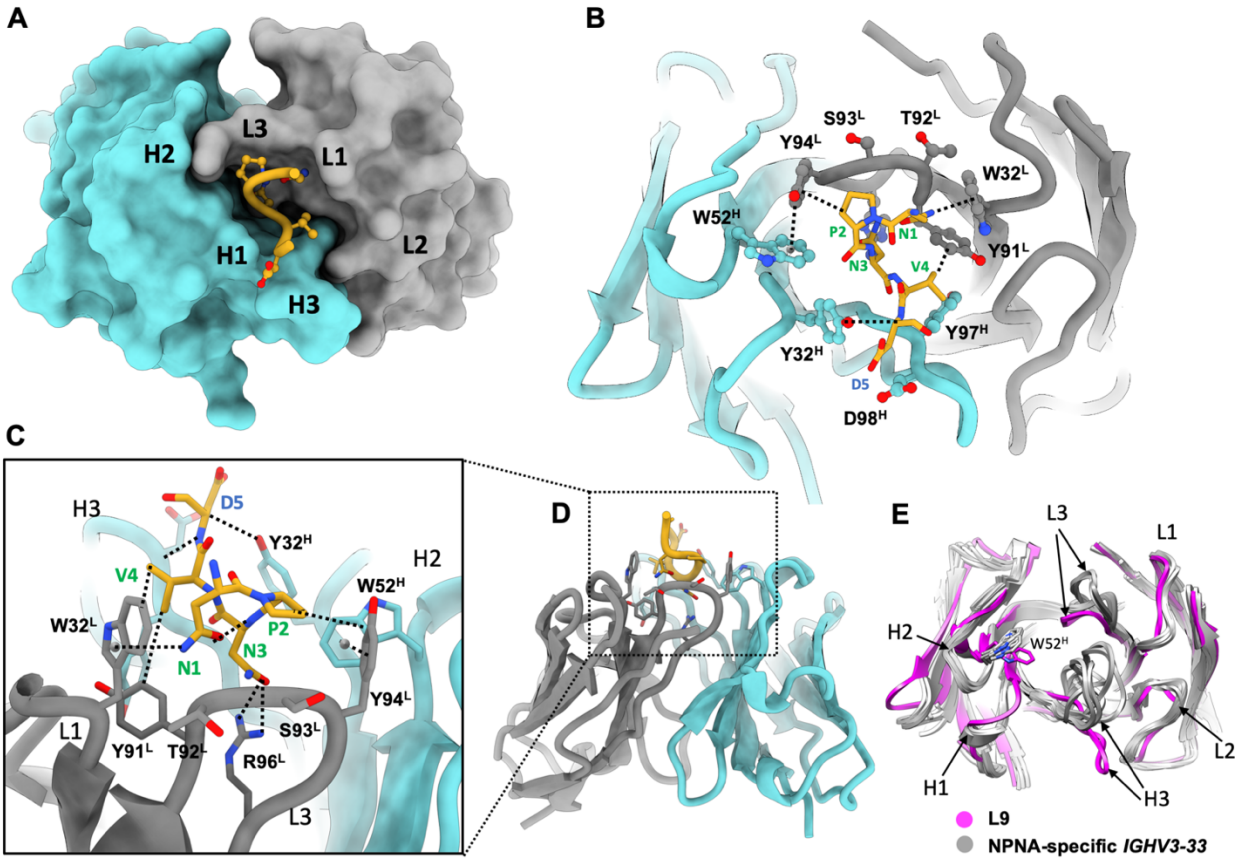

Figure 2. The L9 PfCSP epitope comprises NPNVD. (A) Surface representation of L9 Fab, with central NPNVD shown in gold. CDR loops are specified. **(B)** Structural details of CSP binding pocket. Key interactions are highlighted with dashed lines. **(C)** Rotated view of (B), zoomed in from (D). **(D)** Rotated view of (A), shown in ribbon diagram. **(E)** Alignment of L9 Fab (magenta) with a panel of NPNA-specific *IGHV3-33* Fabs; sequences in fig. S5.

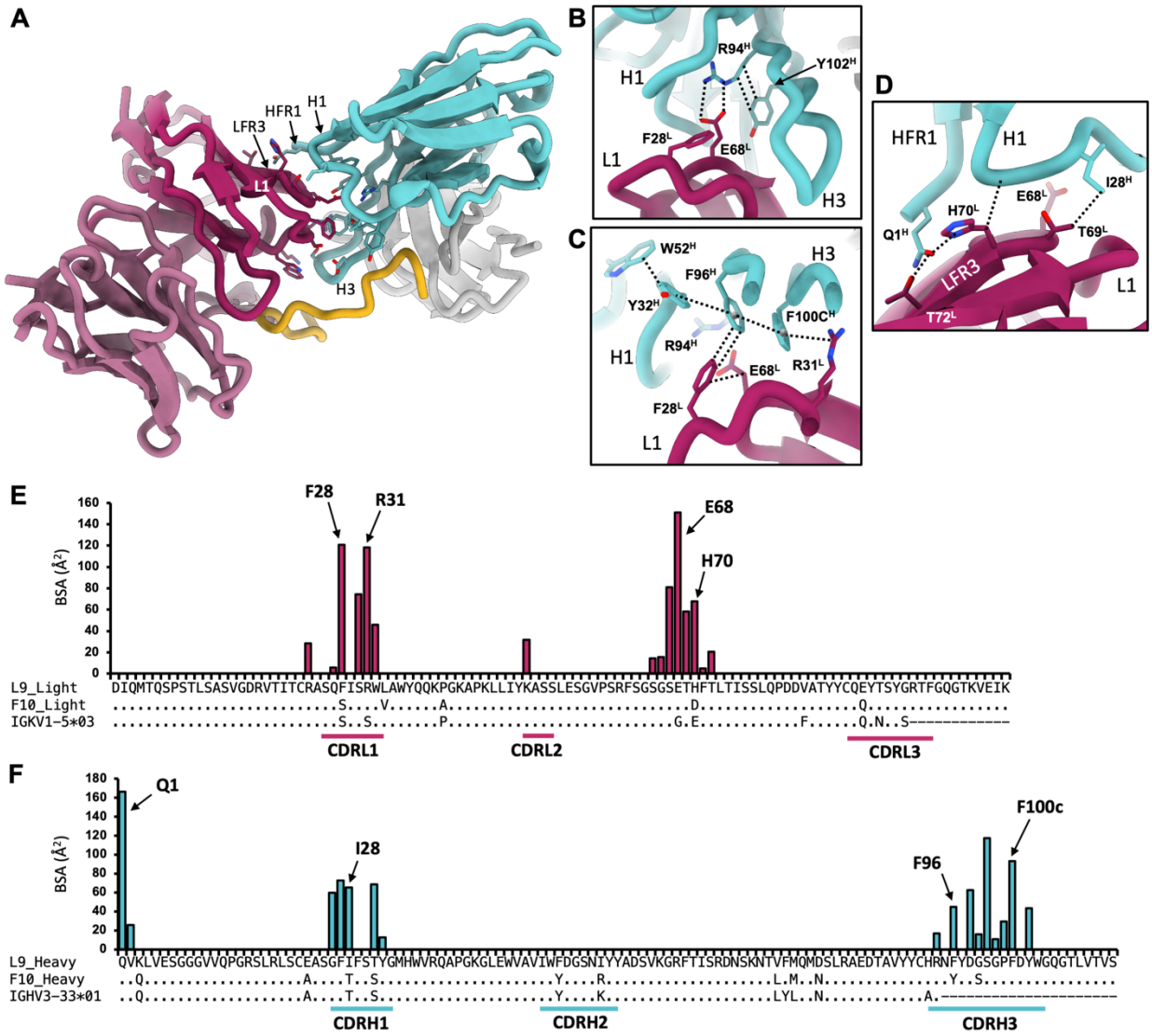

Figure 3. L9$_K$ mediates extensive homotypic interactions. (A) Ribbon diagram of Fab B (cyan) and C (maroon); side chains of interacting residues are shown. **(B-D)** Structural details of key homotypic interactions. Dashed lines indicate specific contacts. **(E)** Buried surface area (BSA) contributions of individual residues to the homotypic interface in L9 light chain. Sequence alignment with F10$_K$ and germline *IGKV1-5* gene is shown below. **(F)** Same as in (E), for L9 heavy chain, with sequence alignment to F10$_H$ and germline *IGHV3-33* gene.

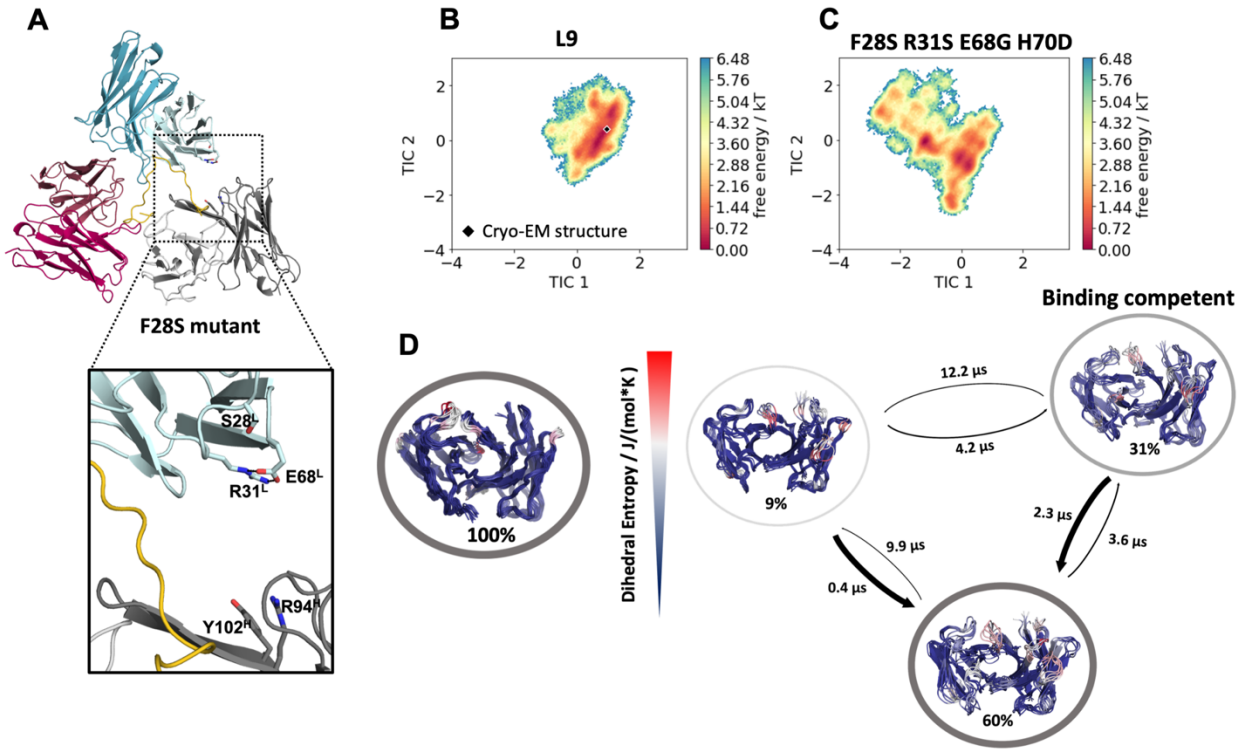

355

356 **Figure 4. Molecular dynamics reveals $L9_K$ residues critical for stability of the homotypic**
357 **interface and CSP binding. (A)** Most populated structure for the F28S variant, highlighting the
358 loss of critical homotypic interactions. **(B-C)** Free energy landscapes of the L9 WT and
359 the F28S/R31S/E68G/H70E variant projected in the same coordinate system, revealing a
360 substantial increase in conformational space and a population shift due to the mutations. Cryo-
361 EM structure is depicted as black diamond. **(D)** Conformational ensemble representatives, state
362 probabilities and transition kinetics for the WT and the quadruple mutant, color-coded according
363 to their dihedral entropy (blue-low flexibility, red-high variability).

364